JPL PUBLICATION 79-59

Processing of Multispectral Thermal IR Data for Geologic Applications

Anne B. Kahle
Daryl P. Madura
James M. Soha

November 15, 1979

National Aeronautics and
Space Administration

Jet Propulsion Laboratory
California Institute of Technology
Pasadena, California

CONTENTS

Introduction 1

Image Processing 3

A Geometric Corrections 3

B. Contrast Enhancement and Color Display 3

C. Band Ratioing 9

D. Sensor Calibration, Atmospheric Corrections and Derivation of Emittance 11

E. Color Enhancement 25

References 38

Tables

I. Mid-IR Channels on 24-Channel Scanner 3

II. Atmospheric Parameters from LOWTRAN 4 16

Figures

1. Geometrically corrected, contrast-enhanced original images 5

2. Color composite of channels 17, 18 and 20, rectified to map base and individually contrast-enhanced as in Figure 1 7

3. Ratios 17/18, 18/19, 19/20, 20/21, and 21/22 individually contrast stretched 10

4. Color ratio composite of ratios 17/18, 18/19, and 19/20 as blue, green and red respectively 13

5. Temperature image derived from assumption that ε_{21} = constant = 0.93 21

6. Emittance images for channel 17, 18, 19 and 20 using temperature from Figure 5 22

7. Emittance color composite using channels 17, 18 and 20 as blue, green and red, respectively 23

8. Color-enhanced emittance composite 27

9. Color-enhanced radiance composite 29

10. Two-dimensional histogram plotting data distribution of channel 17 vs channel 18 32

ABSTRACT

Multispectral thermal IR data were acquired with NASA's Bendix 24-channel scanner flown in an aircraft over the E. Tintic Utah mining district. These digital image data required extensive computer processing in order to put the information into a format useful for a geologic photo-interpreter. Simple enhancement procedures were not sufficient to reveal the total information content because the data were highly correlated in all channels. The data were shown to be dominated by temperature variations across the scene, while we were interested in the much more subtle spectral variations between the different rock types. In this paper we discuss the image processing techniques employed to analyze these data.

The first step was to create a view-angle-corrected image from each tape to evaluate data quality and select the area of interest. Next, following the work of Vincent and Thomson (1972), ratio images were produced for each pair of adjacent wavelength channels, and a color ratio composite created. To quantify the data further, on-board sensor calibration and an atmospheric model utilizing Salt Lake City radiosonde data were used to determine the surface brightness temperature from the 11-12 μm channel. This surface brightness temperature, combined with the calibration and atmospheric model, was then used to create emissivity images for each of the remaining wavelength channels. A color ratio composite of three emissivity images provided improved separation but was not fully satisfactory, due in part to increased noise. Finally a principal component transformation, followed by a Gaussian stretch, followed by an inverse transformation to the original axes achieved satisfactory separation of many of the major rock types. This procedure was invoked for both the raw radiance data and the emissivity images. While both

revealed about the same amount of rock-type information, the former was judged to be much easier to interpret because of the topographic information intrinsic in the temperature was still contained in the final product.

INTRODUCTION

Laboratory measurements of middle-infrared (MIR, 5-40 μm) spectra of rocks and minerals show numerous diagnostic features. The region between 8 and 14 μm holds the most promise for remote sensing because this is an excellent atmospheric window and also the region of maximum thermal emission at terrestrial surface temperatures. Within this spectral range, the most prominant spectral features arise from the silicon-oxygen stretching vibrations. These features change location and intensity with varying composition and structure (Hunt and Salisbury, 1974, 1975, 1976; Vincent et al., 1975). Lyon (1965) indicated that these intense features (known as reststrahlen bands in reflectance spectra) shift to shorter wavelengths with increasing silica content.

The possibility of exploiting these spectral features for remote sensing of rock-type from aircraft or satellite has been suggested by numerous authors (Vickers and Lyon, 1967; Vincent and Thomson, 1972; Vincent, 1975). However, owing to lack of multispectral scanners (Vincent, 1975), very few tests of the technique have been possible. Hovis et al. (1968) flew a non-imaging emittance spectrometer over desert terrain in California. They concluded that even though atmospheric effects were significant, the reststrahlen bands of silicates were observable. Lyon (1972) flew a non-imaging spectrometer over the Pisgah lava flows and surroundings. He was able to distinguish between the basalts, the alluvial fans, and the windblown sands, and also recognized spectral differences within the basalt flows. Two tests with a two-channel imaging spectrometer have been reported. Vincent et al., 1972, flew a scanner with a band between 8.2 and 10.9 μm and another band between 9.4 and 12.1 μm, over a sand quarry near Mill Creek, Oklahoma. By band ratioing, they produced

images on which they could distinguish between the quartz sand or sandstone, and the non-silicate surface material. Vincent and Thomson (1972) flying a scanner with the same two channels over the Pisgah Crater area were able to discriminate dacite from basalt, and a rhyolitic tuff was distinguished from the surrounding alluvium. However, until recently, lack of adequate imaging multispectral scanners has precluded further validation of the use of spectral emittance data.

In November of 1975, NASA's 24-channel scanner was flown over the East Tintic mining district of central Utah. On this flight six channels of radiance data were acquired in the 8.27 to 13 μm range. This flight provided an unprecedented opportunity to analyze multispectral mid-IR image data in an area of moderate geologic complexity. The district, in an area of high relief and moderate vegetation, consists mainly of Tertiary silicic igneous rocks and Paleozoic quartzite and carbonate rocks which have been locally hydrothermally altered.

Improved image processing algorithms were required to best utilize these data sets. Simple contrast enhancement and color compositing of the various spectral channels were insufficient to reveal the information content, because the data were highly correlated in all channels. The data were dominated by temperature variations across the scene, while we were interested in the much more subtle spectral variations between the different rock types. This paper describes the image processing applied to these data sets, with illustrations of most of the data products. The geologic interpretation of the images, along with the supporting field and lab work will be discussed elsewhere.

IMAGE PROCESSING

A. Geometric Corrections

The raw data used in this study were obtained by NASA's Bendix 24-channel scanner. Three parallel flight lines were flown, with the aircraft at an elevation of between 5000 m and 6000 m above the terrain. The total of 12 computer compatible tapes (CCT's) were produced at Johnson Space Center, with each tape containing all 24 channels (operative or not) for a portion of a flightline. Each picture element on the original data covered a ground area of approximately 10 by 10 m at the sub-aircraft point.

Because the recorded data values represented radiance measurements for equal angular displacements of the scanning apparatus, a panorama correction was applied immediately after logging the data. To accomplish this correction, the raw data were resampled along each scan line such that each data value represented the same surface area, as described by Gillespie and Kahle (1977).

B. Contrast Enhancement and Color Display

Of the 24 channels, there were six operational channels in the mid-IR wavelength. Table I shows the position and effective bandwidths in the electromagnetic spectrum of these channels.

Table I
Mid-IR Channels on 24-Channel Scanner

Channel	Bandlimits (micrometers)
17	8.3 - 8.8
18	8.8 - 9.3
19	9.3 - 9.8
20	10.1 - 11.0
21	11.0 - 12.0
22	12.0 - 13.0

The images of the ground scene for these six channels were individually contrast enhanced, and those from one tape near the center of the test area are displayed in Figure 1. The contrast enhancement used here was obtained by matching the cumulative distribution functions of each of the six channels to a reference truncated Gaussian distribution of $\pm$ 2.0 σ.

It is immediately apparent in Figure 1 that surface temperature, controlled by topography, is the dominant information in these images. Only very minor changes can be detected between images. Channel 22 has noticeable noise striping.

In order to better perceive subtle brightness changes in the scene, it is customary to combine three of the images into a single color display. This is accomplished by assigning each image a primary color and simultaneously projecting all three images onto color film. Figure 2 illustrates this process using channels 17, 18, and 20 as blue, green, and red respectively. The original radiance data had some areas that were saturated, i.e., the ground temperature was either too hot or too cold for the measured radiance to lie within the range of the recording system. While these areas appeared either white or black in the data displayed in Figure 1, we have set all these areas to black in the color composite, Figure 2, and have done so in most subsequent images.

In order to compare directly the processed images with geologic information, a registration procedure was carried out using the Universal Transverse Mercator (UTM) grid system. First the image displayed in Figure 1 was concatenated with the image of the area lying just to the north. Tiepoints were then chosen that could be identified both on this large image and on the USGS topographic map of the area. On the image, the tiepoints were referenced by their line and sample coordinates and on the map by their UTM coordinates.

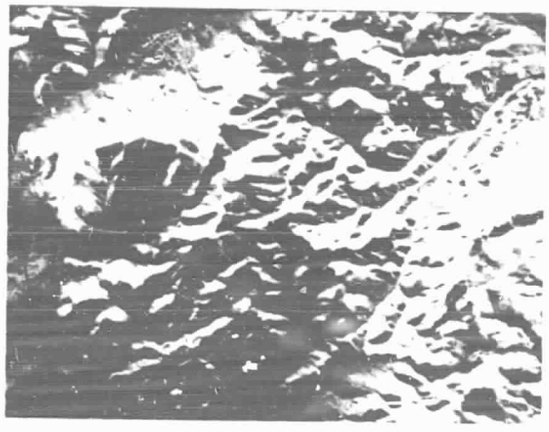

a. Channel 17

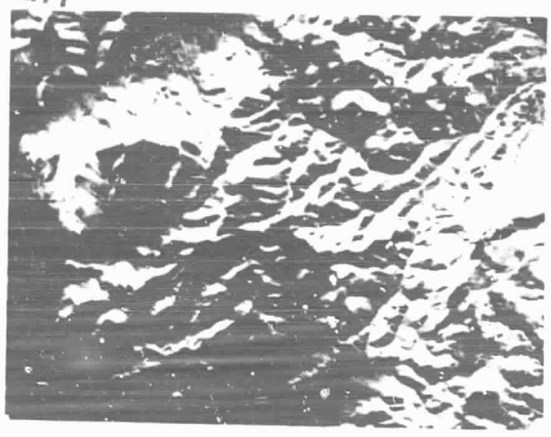

b. Channel 18

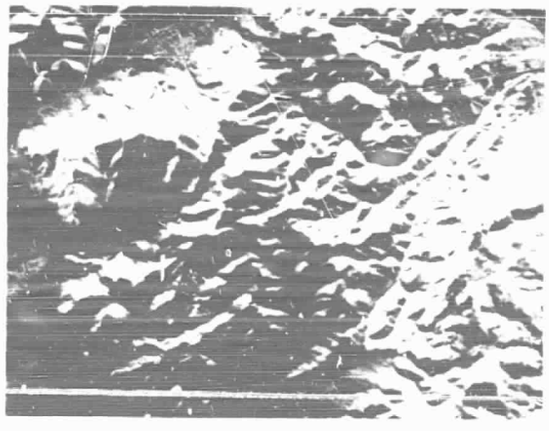

c. Channel 19

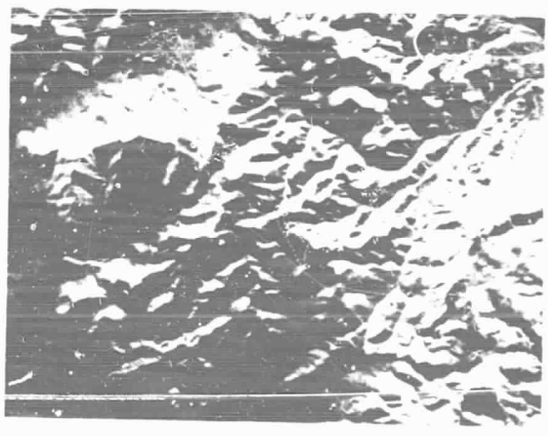

d. Channel 20

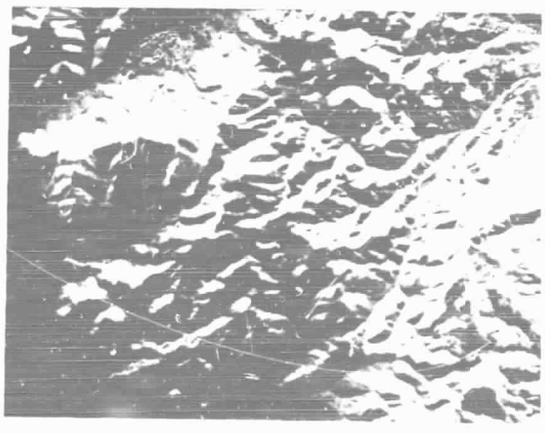

e. Channel 21

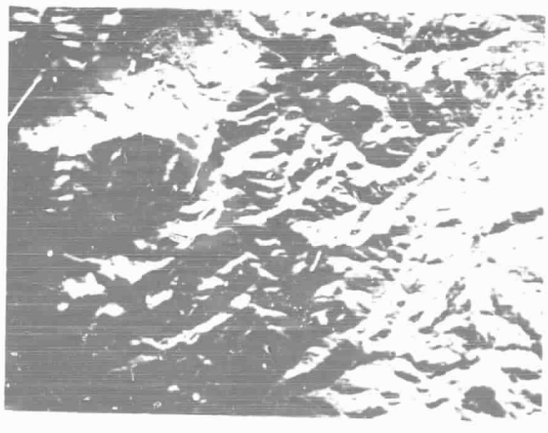

f. Channel 22

Figure 1. Geometrically corrected, contrast-enhanced original images.

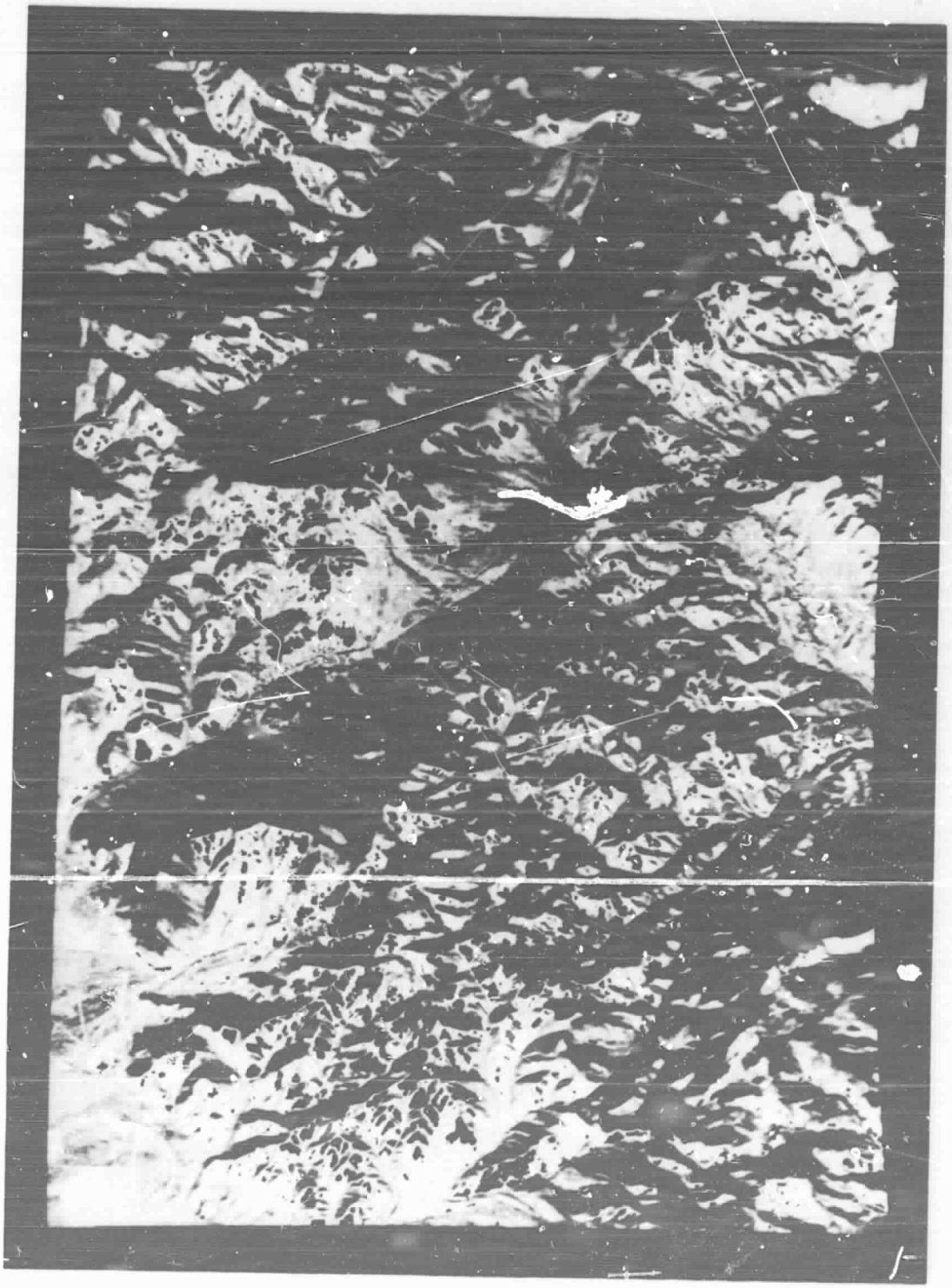

Figure 2. Color composite of channels 17, 18 and 20, rectified to map base and individually contrast-enhanced as in Figure 1.

The set of tiepoints was used to determine a second order polynomial transformation which mapped the line and sample tiepoint coordinates to their respective UTM coordinates. Using this polynominal transformation, a regular tiepoint grid was generated that covered the entire image. The displacements associated with the grid points then controlled a geometric transformation algorithm by which the full image was resampled. Figure 2 and all subsequent color images display the results of this geometric transformation.

In Figure 2 we note that the dominance of temperature effects, with the resulting high inter-band correlation, causes the range of color to be quite low. Nevertheless it is possible to recognize the location of the Tintic Quartzite -- the distinctive pink unit along the left edge of the image. Beyond that distinction we see only that the image is divided into light pink or gray green.

C. Band Ratioing

One technique used to deal with the problem of high correlation between channels is to create ratios of one channel to another (Vincent and Thomson, 1972; Vincent, 1973). In this way, the temperature effects tend to cancel out. However, because of the high inter-band correlation, the resultant ratio images have very narrow distributions of data values centered about unity. When these ratio images are contrast enhanced for display purposes, high gains must be applied in order to produce images utilizing the full black to white brightness range. Because random noise is intrinsically uncorrelated from channel to channel, the above procedure reduces the apparent signal-to-noise ratio. Consequently, the application of large gains to the ratio images tends to emphasize the uncorrelated noise, as can be seen in Figure 3 which displays the ratio images of adjacent bands: 17/18, 18/19, 19/20, 20/21, and 21/22. As before, it is useful to construct a single color display, this time using

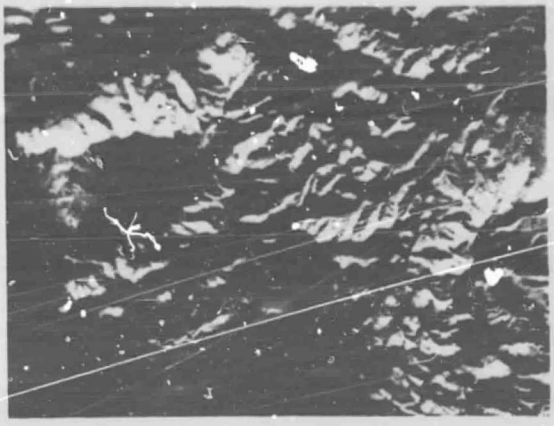

a. 17/18

b. 18/19

c. 19/20

d. 20/21

e. 21/22

Figure 3. Ratios 17/18, 18/19, 19/20, 20/21, and 21/22 individually contrast stretched.

three ratio images. Figure 4 displays the color ratio composite using 17/18, 18/19, 19/20, as blue, green and red respectively. In this image more color separation has become apparent. The Tintic Quartzite along with other quartz-rich rocks are a deep purple. However, the rust colored areas and green areas each consist of several rock types, alluvial material, and/or vegetation. The magenta appears to be temperature related, appearing primarily on cool north-facing slopes.

D. Sensor Calibration, Atmospheric Corrections and Derivation of Emittance

The black and white images above, together with the associated color composites represent the initial products that were created. The existence of onboard calibration equipment made it possible to generate a physically meaningful quantity, the surface spectral emittance, which potentially might be more directly interpretable. We use the term emittance, rather than emissivity, to indicate that we are considering a surface in its natural state, rather than an ideal specimen. To determine the emittance value corresponding to a given raw data value required a simple atmospheric model which provided average values in each channel of atmospheric transmission, emission, and scattering properties. Using the onboard calibration and the atmospheric model, it is possible, as described below, to determine the surface temperature at every data point if we assume that the emittance in the longest wavelength channel (12 - 13 μm) is constant across the entire image (Lyon, 1965; Vincent, 1972). Once this temperature is known, it is then possible to calculate the surface emissivity for every point in the scene for each of the remaining wavelength channels.

Following the notation of Vincent and Thomson (p. 2467) the total spectral radiance at the sensor for the wavelength λ is given by

Figure 4. Color ratio composite of ratios 17/18, 18/19 and 19/20 as blue, green and red, respectively.

$$L_\lambda = [\varepsilon_\lambda L_{bb\lambda}(T) + (1 - \varepsilon_\lambda) L_{sky\lambda}] \tau_{A\lambda} + L_{v\lambda} \quad (1)$$

where

ε_λ is the surface emittance,

$L_{bb\lambda}(T)$ is the spectral radiance of a black body at surface temperature T,

$L_{sky\lambda}$ is the spectral radiance incident upon the surface, from the atmosphere,

$\tau_{A\lambda}$ is the spectral atmospheric transmissivity,

$L_{v\lambda}$ is the spectral radiance from atmospheric emission and scattering that reaches the sensor.

In this study, equation (1) is utilized in an average sense. That is, it is written once for each channel, using the average values from the atmosphere model for $L_{sky\lambda}$, $\tau_{A\lambda}$, and $L_{v\lambda}$. The intent is to be able to solve the equation for the average emittance at each data point in the image for all the thermal channels. For a given data point, these average emittances can then be plotted as a function of wavelength. The atmospheric model employed was LOWTRAN 4 (Selby, et al., 1978). Salt Lake City radiosonde data for the day of the overflight was used in the model to define atmospheric conditions. The model then produced atmospheric transmissivity, $\tau_{A\lambda}$, atmospheric directional upward radiance, $L_{v\lambda}$, and directional downward radiance. The latter was integrated over the sky hemisphere to determine the downward radiance at the surface, $L_{sky\lambda}$. These quantities are given in Table II.

Table II

Atmospheric Parameters from LOWTRAN 4

Wavelength Interval (μm)	$\tau_{A\lambda}$	$L_{sky\lambda}$ (watts/m^2 sr μm)	$L_{v\lambda}$ (watts/m^2 sr μm)
8.3 - 8.8	0.848	4.198	0.962
8.8 - 9.3	0.885	3.286	0.650
9.3 - 9.8	0.801	5.116	1.180
10.1 - 11.0	0.910	3.248	0.603
11.0 - 12.0	0.912	2.696	0.498
12.0 - 13.0	0.816	4.945	1.143

Referring back to equation (1), once the atmospheric parameters are defined, the remaining unknowns are the surface emittance, ε_λ and the surface temperature T. $L_{bb\lambda}(T)$ can be calculated using Planck's blackbody radiation function once T is known. The following derivation illustrates how a corresponding surface temperature image may be constructed using the calibration information provided and one of the thermal channels.

For a given thermal channel i, the relative sensor response $R^i(\lambda)$ has a Gaussian-like form with response falling to zero at the extremes λ_1^i and λ_2^i (i.e. $R^i(\lambda) = 0$ for $\lambda \leq \lambda_1^i$ and $\lambda \geq \lambda_2^i$). The wavelength intervals given in Table II are the approximate domains for which $R^i(\lambda)$ is greater than half its maximum value.

To deal with the non-uniform sensor response, all spectral radiance functions in equation (1) are weighted by the relative filter response $R^i(\lambda)$ and integrated over the bandpass to obtain an effective radiance value

$$\bar{L}^i = \frac{1}{N^i} \int_{\lambda_1^i}^{\lambda_2^i} R^i(\lambda)\, L^i(\lambda)\, d\lambda \qquad (2)$$

where the overbar will be used to denote effective radiance. The normalization constant N^i is chosen to make the effective radiance equal to that value

of constant spectral radiance which would produce an equivalent respo.se in the sensor. This constant is then

$$N^i = \int_{\lambda_2^i}^{\lambda_1^i} R^i(\lambda)\, d\lambda$$

The response of the sensor in terms of output data value (DV) is then assumed to be a linear function of this effective radiance according to

$$DV^i = A_i \bar{L}^i + B_i \tag{3}$$

The radiance of a blackbody source at temperature T is given by

$$L_{bb}^i(\lambda,T) = \frac{c_1}{\pi\lambda^5 (e^{c_2/\lambda T} - 1)} \frac{\text{watt}}{m^2 \text{ sr}}$$

where

c_1 = first radiation constant = 3.74×10^{-16} watt m^2,

c_2 = second radiation constant = 0.0144 m^oK.

Then the effective or normalized radiance from a blackbody source in the same wavelength region is given by applying equation (2)

$$\bar{L}_{bb}^i(T) = \frac{1}{\pi N^i} \int_{\lambda_1^i}^{\lambda_2^i} \frac{c_1 R^i(\lambda) d\lambda}{\lambda^5 (e^{c_2/\lambda T} - 1)} \tag{4}$$

The calibration system consisted of two blackbody sources maintained at different, known temperatures. After the completion of each scan line of the ground scene, the two blackbodies were scanned and the corresponding data values were recorded along with temperature. Let the temperature of the colder blackbody be T_C and that of the hotter blackbody be T_H. The two cali-

bration points then become

$$[DV_C^i, \bar{L}_{bb}^i (T_C)], [DV_H^i, \bar{L}_{bb}^i (T_H)]$$

where the blackbody effective radiances $\bar{L}_{bb}^i (T_C)$ and $\bar{L}_{bb}^i(T_H)$ are calculated according to equation (4). Using the linear sensor response model of equation (3), a system of two equations is generated

$$DV_C^i = A_i \bar{L}_{bb}^i (T_C) + B_i$$

$$DV_H^i = A_i \bar{L}_{bb}^i (T_H) + B_i$$

which can easily be solved for the coefficients A_i and B_i.

When the scanner samples the actual surface, all the radiance terms of equation (1) influence sensor response, so the linear sensor model becomes

$$DV^i = A_i \bar{L}_{tot}^i (T,\varepsilon_i) + B_i \tag{5}$$

where

$$\bar{L}_{tot}^i (T,\varepsilon_i) = \varepsilon_i \tau_A^i \bar{L}_{bb}^i (T) + (1-\varepsilon_i) \tau_A^i \bar{L}_{sky}^i + \bar{L}_v^i \tag{6}$$

The latter expression is obtained by applying equation (2) to the right side of equation (1). The blackbody effective radiance $\bar{L}_{bb}^i(T)$ is determined according to equation (4). The other two effective radiance terms are easily

related to the values in Table II by assuming $L_{sky\lambda}$ and $L_{v\lambda}$ are constant through the wavelength region. Thus

$$\bar{L}^i_{sky} = \frac{1}{N^i} \int_{\lambda_1^i}^{\lambda_2^i} R^i(\lambda)\, L^i_{sky\lambda}\, d\lambda$$

$$= \frac{L^i_{sky\lambda}}{N^i} \int_{\lambda_1^i}^{\lambda_2^i} R^i(\lambda)\, d\lambda = L^i_{sky\lambda}$$

and similarly,

$$\bar{L}^i_v = L^i_{v\lambda}$$

From laboratory spectra, Vincent et al., 1975 state that in the 12 - 13 μm region, the emittance of many silicate igneous rocks approaches a constant values (≈0.96). This wavelength region corresponds to channel 22. If this result is applied to equation (5):

$$DV^{22} = A_{22}\, \bar{L}^{22}_{tot}\, (T, \varepsilon_{22} \approx 0.96) + B_{22} \qquad (7)$$

We now have an expression involving only data values and temperature. Since the temperature T cannot be solved for analytically, a numerical inversion technique was employed. The signal level, DV^{22}, was calculated from equation (7) for a sufficiently broad range of temperatures to encompass the allowable range of DV. This information was stored in tabular form. The table was then inverted by interpolation, yielding a temperature value for each possible value of DV^{22}. The table was then referenced for each picture element to produce a temperature image.

The emittance values for channels 17 - 21 could then be determined in the following manner. Suppose that the constants A_i and B_i were determined as before. Solving equation (6) for $\bar{L}^i_{tot}(T,\varepsilon_i)$:

$$\bar{L}^i_{tot}(T,\varepsilon_i) = \frac{1}{A_i} \quad (DV^i - B_i)$$

Substituting into equation (4) and solving for ε_i gives:

$$\varepsilon_i = \left[\frac{1}{\bar{L}^i_{bb}(T) \cdot \tau^i_A - \bar{L}^i_{sky} \cdot \tau^i_A}\right]\left[\frac{1}{A_i}(DV^i - B_i) - \bar{L}^i_v - \tau^i_A \cdot \bar{L}^i_{sky}\right]$$

Now, at each data point in the image, T has already been determined and DV^i is known. So, the emittance at that data point is completely determined. In this manner, the corresponding emittance images for each of channels 17 through 21 can be determined using the temperature image created from channel 22 along with the calibration information. (Note again that the emittance for channel 22 is assumed to be constant.)

With the available data, channel 22 was of such poor quality that using it to generate the temperature image resulted in unacceptably noisy emittance images. Channel 21 was used instead, with $\varepsilon_{21} = 0.93$, but assuming a constant emittance for this channel is questionable. In this wavelength region (11 - 12 μm) many of the silicates have a steeply rising spectrum, and the carbonates have a narrow but intense band (Hunt and Salisbury, 1974, 1975, 1976). Nevertheless, use of channel 21 was considered to be preferable to use of channel 22 with its excessive noise. The temperature image based on this calculation is shown in Figure 5. Figure 6 displays contrast enhanced emittance images for channels 17, 18, 19, and 20, derived using channel 21 to generate the temperature image. Figure 7 is a color composite formed using

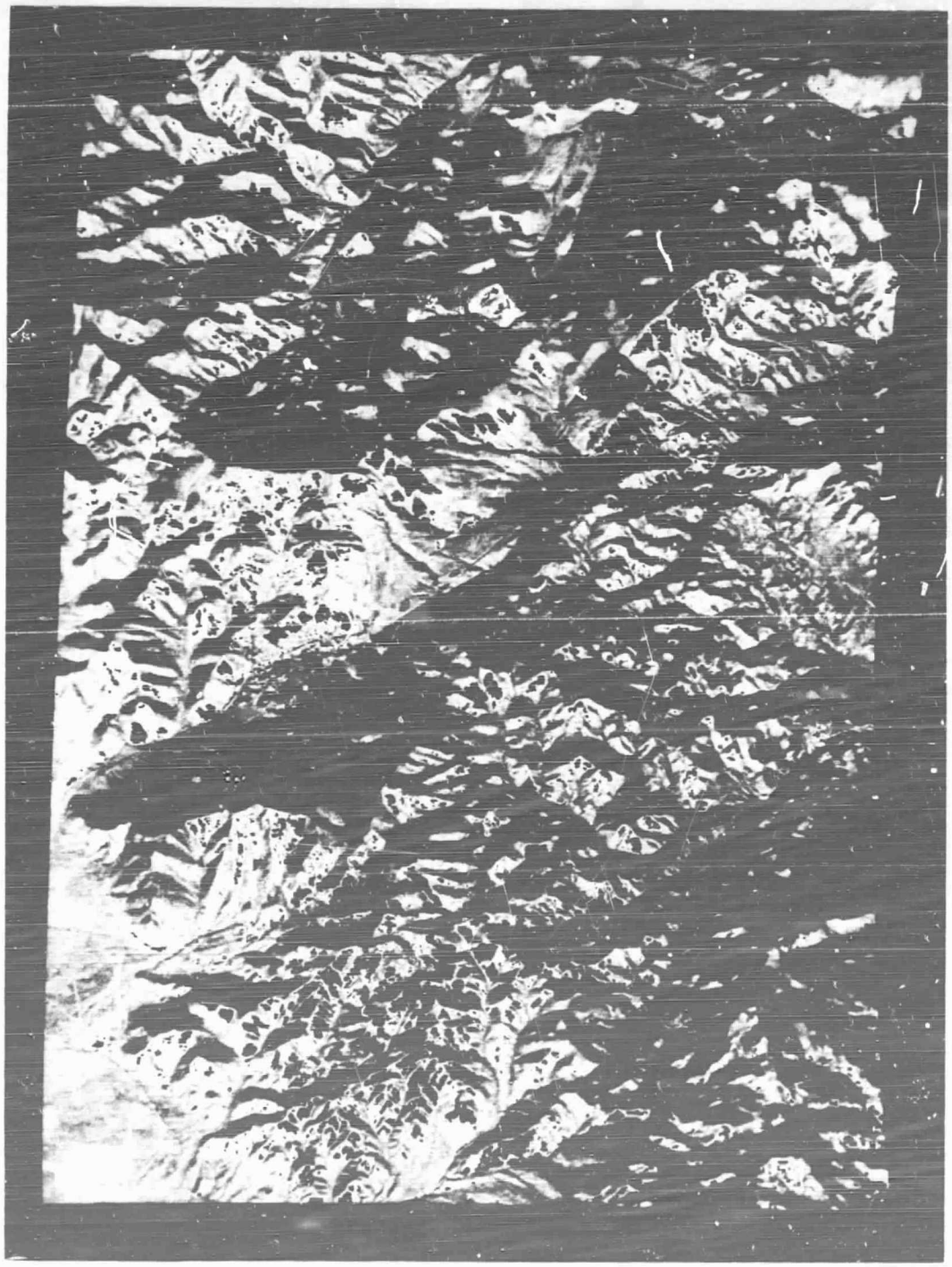

Figure 5. Temperature image derived from assumption that ε_{21} = constant = 0.93.

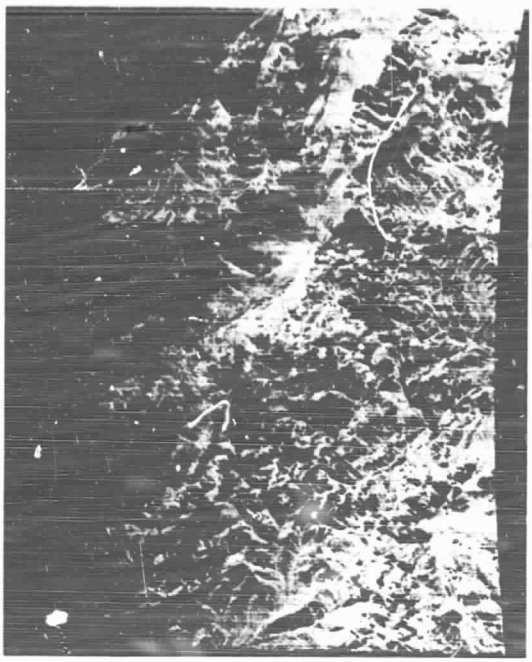

a. Channel 17

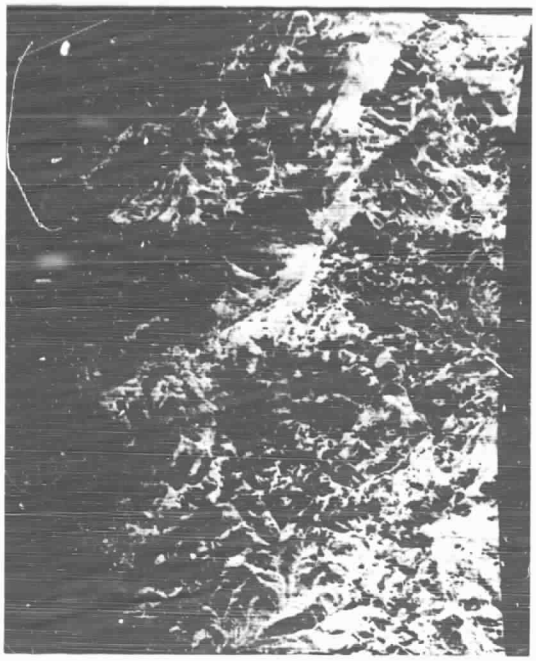

b. Channel 18

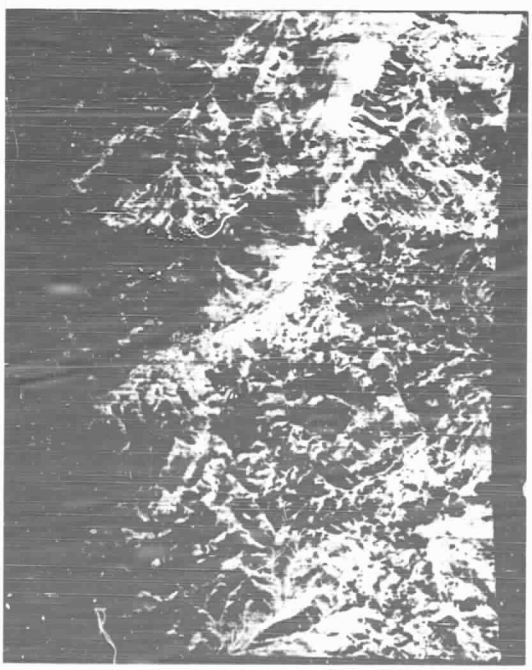

c. Channel 19

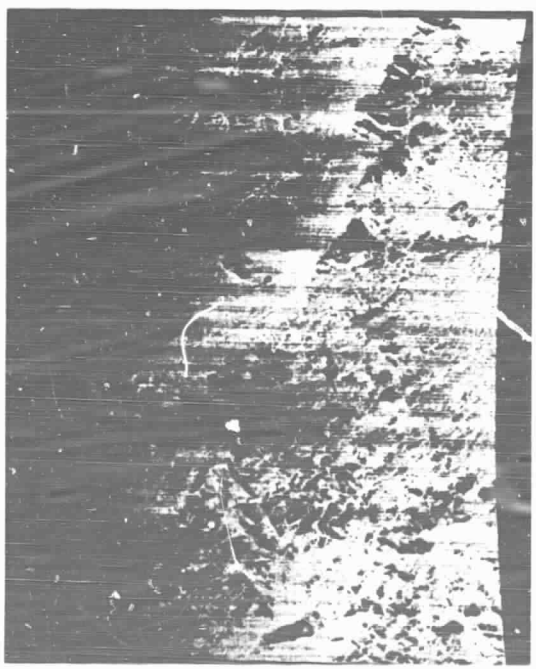

d. Channel 20

Figure 6. Emittance images for channel 17, 18, 19, and 20 using temperature from Figure 5.

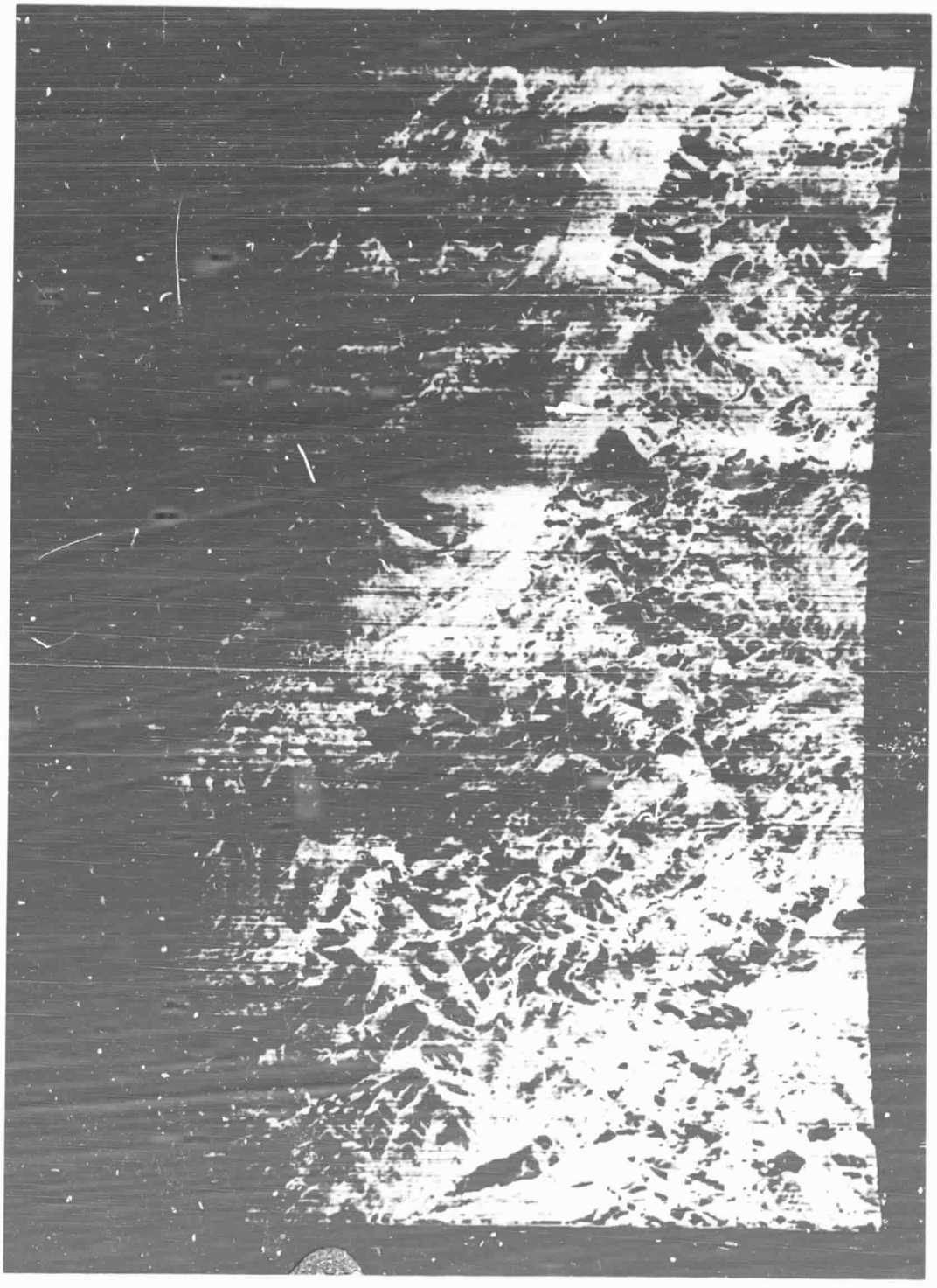

Figure 7. Emittance color composite, using channels 17, 18 and 20 as blue, green and red, respectively.

channels 17, 18, and 20 of the above emittance images displayed as blue, green, and red respectively.

In the individual channel emittance images, it is apparent that the quartzite (left center) has low relative emittance in all wavelength channels, although not as pronounced in the highest wavelength. Discrimination of the rock units does not appear to be based upon the moving of the reststrahlen band to higher wavelength with decreasing silica content so much as just the existence of a very broad intense spectral feature across all wavelengths in the high quartz content rocks. In the color composite emittance image quite a bit of rock type discrimination has become possible, as will be discussed further with Figures 8 and 9.

Several other atmospheric models and several values of constant emissivity for channel 21 were used in the foregoing derivation of emissivity images. The changes in constant emissivity value had no noticeable effect on the emissivity images -- merely raising or lowering the absolute value of the derived emissivity values. Evaluation of the emissivity images derived using different atmospheres show minor but not significant changes. Ability to distinguish geologic units was unchanged.

E. Color Enhancement

As is apparent, particularly in Figure 2, but also in Figures 4 and 7, a problem associated with highly correlated multispectral data is a lack of color range in a color composite display. This problem was solved for the emittance and thermal radiance composites by use of a multispectral transformation technique that removes correlation between components without rotating the data distribution.

The simplest and most frequently used approach to enhancement of a color image is to separately perform contrast enhancement on each individual image

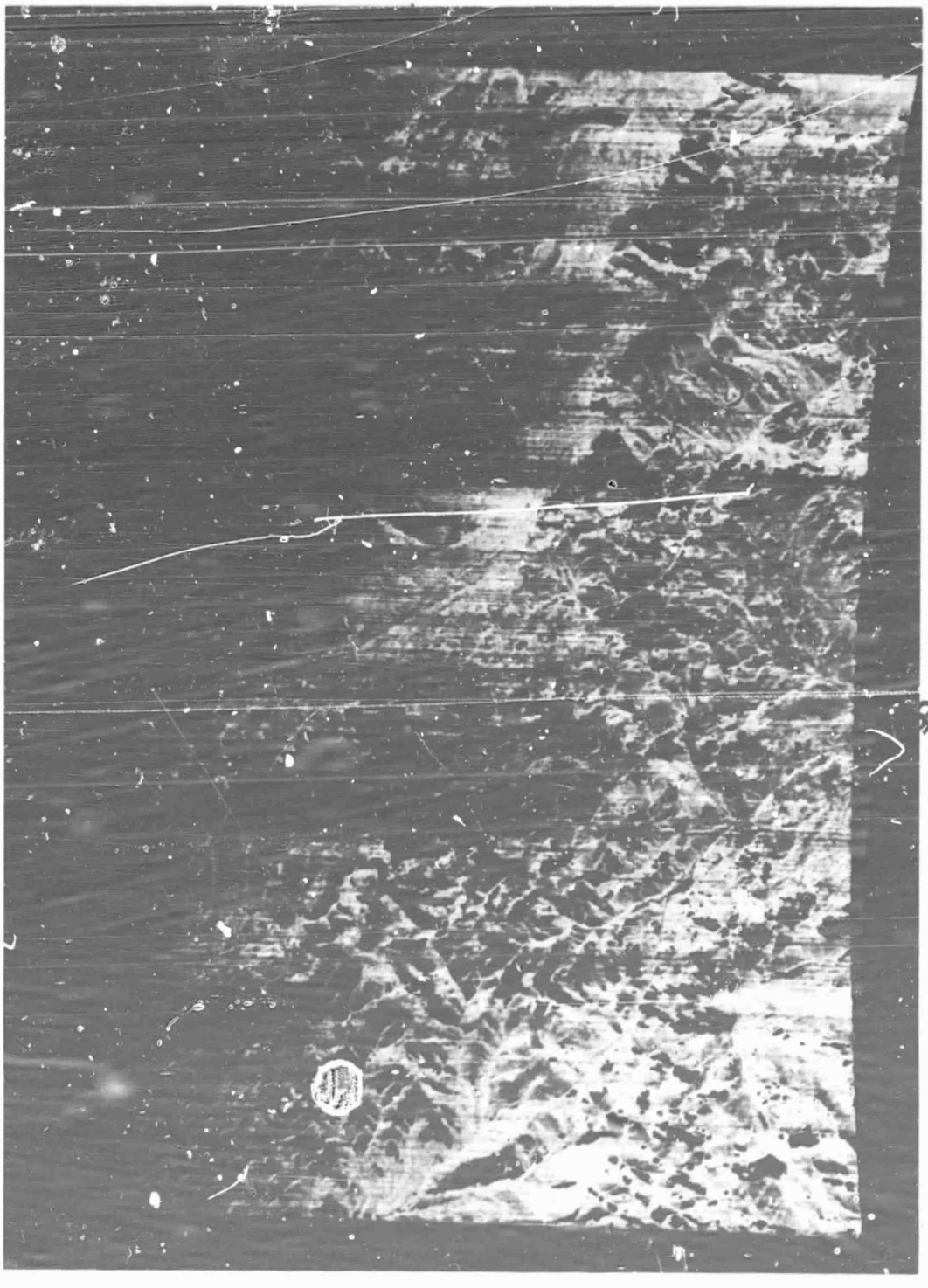

Figure 8. Color enhanced emittance composite.

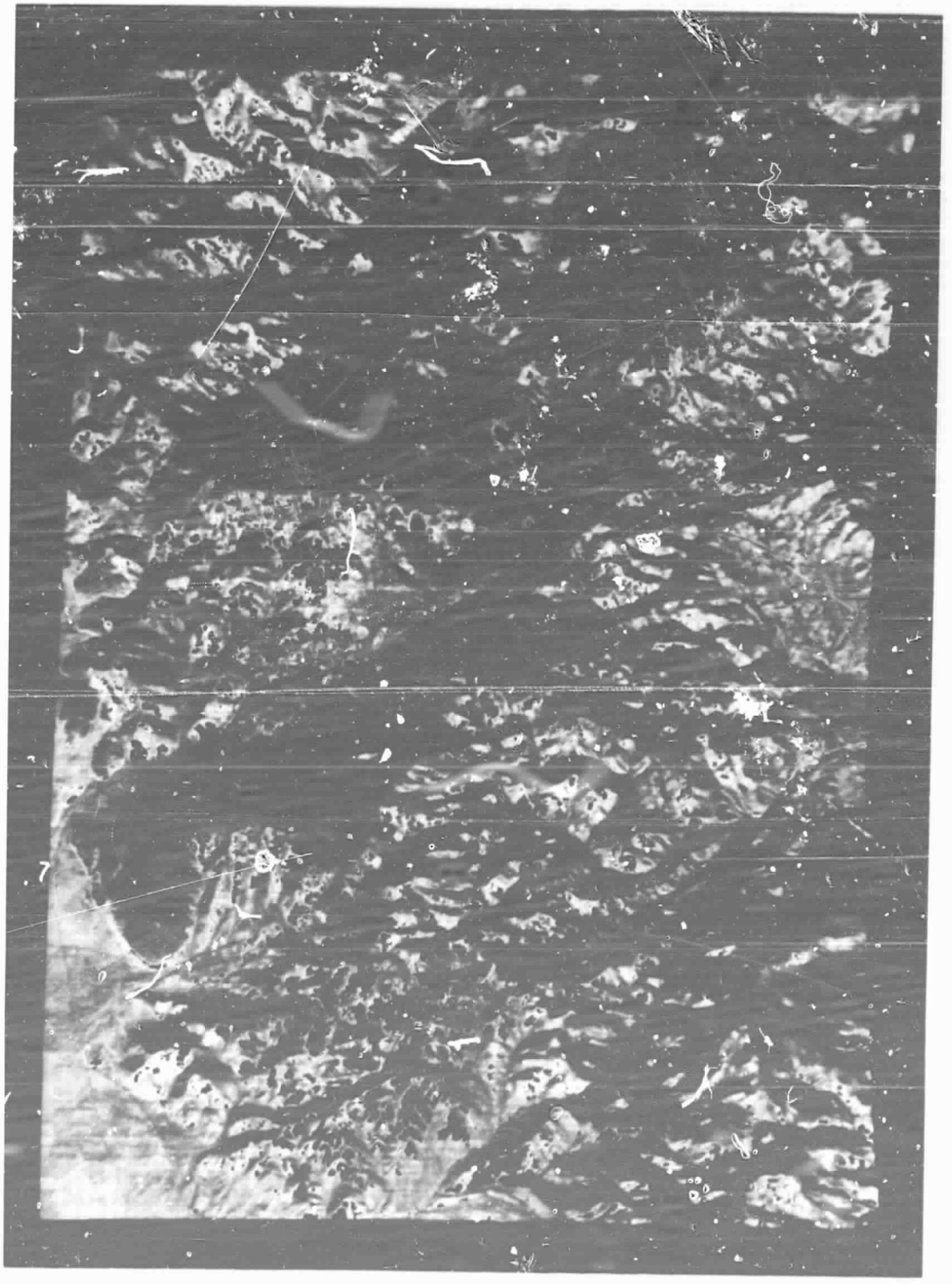

Figure 9. Color enhanced radiance composite.

component. To produce Figure 2, for example, individual intensity transformations

$$Y_i = I_i (x_i)$$

were performed for the i^{th} spectral components (i = 17, 18, 20), where x_i represents the value of an arbitrary picture element in the i^{th} component before enhancement, and Y_i its value after enhancement. For Figure 2, Y_{17} is displayed as blue, Y_{18} as green and Y_{20} as red. For scenes with high interband correlation, separate intensity transformations merely lengthen the narrow extended histogram distribution of the original, without accomplishing the high degree of spreading required to use the full available range of color to display differences in the scene. This situation is illustrated by the two-dimensional histogram of Figure 10. To achieve the needed spreading, joint transformations of the form

$$(Y_{17}, Y_{18}, Y_{20}) = D (x_{17}, x_{18}, x_{20}) \qquad (8)$$

are required.

The technique used to accomplish this joint transformation in the present application involved several steps (Soha and Schwartz, 1978). First, a principal component transformation was applied to the three components (17, 18 and 20) of the emittance image. If we regard the original three components as forming a cartesian 3-space, then the principal component transformation consists of a rotation of the coordinate axes, producing new components which are linear combinations of the original. The transformation is implemented via a 3 x 3 rotation matrix applied to each multispectral picture element vector (x_{17}, x_{18}, x_{20}) to produce three new component images, according to

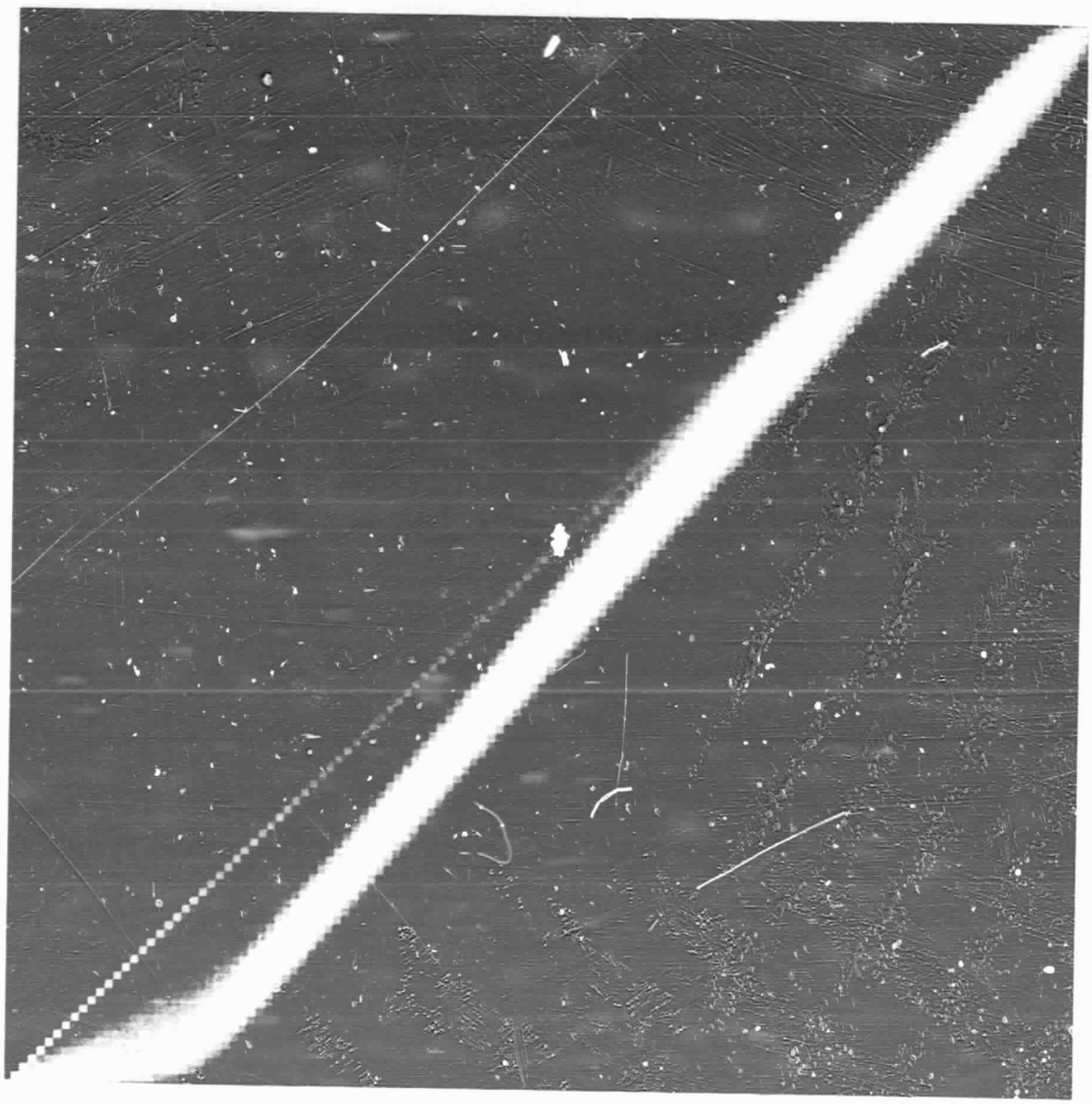

Figure 10. Two dimensional histogram plotting data distribution of channel 17 vs. channel 18.

$$(z_1, z_2, z_3) = P (x_{17}, x_{18}, x_{20})$$

The matrix is derived from the 3 x 3 covariance matrix C, which is estimated over a statistically significant subset of the image by

$$C_{ij} = \frac{\Sigma (x_i - \bar{x}_i) (x_j - \bar{x}_j)}{N}$$

where i, j = 17, 18, 20 and the summation is over N picture elements and $\bar{x}_i$ is the mean value of component i. The diagonal elements of C (with i = j) are the variances of the three components; the off-diagonal elements ($i \neq j$) describe the correlation between components. For highly correlated data, as in Figures 2, 4 and 7, these off-diagonal elements have large absolute values. The difficulty in displaying highly correlated data can be thought of as inefficient use of available display dynamic range: "duplicate" information is displayed in more than one channel, with a resulting waste of potential discriminating power. Fortunately, it is possible to rotate the coordinates to achieve new uncorrelated components. After this rotation P, the covariance matrix C_p relating the new components has no nonzero off-diagonal elements. This new diagonal covariance matrix C_p derives from the original covariance matrix C by a similarity transformation

$$P C P^T = C_p$$

Since C_p is diagonal, both it and the rotation matrix P can be found by solving the eigenvector equation

$$PC = C_P P$$

(Further description of uses of the principal component transformation can be found in Ready and Wintz, 1973.) Production of new uncorrelated components using the principal component transformation P was the first step in the color enhancement procedure.

Next, each rotated component was contrast enhanced, using standard individual intensity transformations. Because the new components are uncorrelated, individual contrast transformations were now capable of producing the desired spreading in the histogram. All components were enhanced (using individual non-linear intensity transformations, collectively referred to as G below) so that their histograms approximated Gaussian distributions of a specified variance, resulting in a three-dimensional composite histogram which approximates a spherically symmetric three-dimensional Gaussian and hence occupies the majority of the available color space.

After the variances of the principal component images have been equalized, it is possible to rotate the "multispectral" coordinates further without re-introducing correlation (Taylor, 1973). To produce the final color enhanced image, a coordinate rotation which is the inverse of the original principal component rotation was applied. Thus the entire joint transformation of equation (8) is defined by

$$D = P^{-1} \cdot G \cdot P$$

The resulting color enhanced product is shown in Figure 8. The inverse rotation can be viewed as returning to the original coordinate orientation. This operation has the advantage of restoring basic color relationships which

existed in the original scene and hence facilitating certain inferences. For example, red areas in Figure 8 result from proportionately lower emittance values in the channel 17 wavelength band.

The same color enhancement procedure was applied to the radiance composite (the data in Figure 2), with the resulting product shown in Figure 9. This product has proven to be preferable for interpretation, primarily because it provides visual separation of topographic and emissivity variations. The first principal component image is a weighted average of the three input thermal radiance channels, and is in fact almost entirely dependent upon ground temperature. When the correlation between the first principal component image and the temperature image of Figure 5 is computed, a correlation coefficient of .967 is found. On the other hand, when the first principal component image is compared to the emissivity images for the channel 17, 18 and 20 wavelength bands, correlation coefficients of less than 0.03 result, indicating little dependence of the first principal component upon emissivity. After the inverse rotation step of the color enhancement procedure, the first principal component, which was very nearly the average of the original components, becomes essentially the intensity component of the final color composite. Since the ground temperature variation of Figure 5 is largely topographically controlled, intensity variation in the final product of Figure 9 results primarily from topography. When the second and third principal component images are compared with the temperature image, minimal correlation coefficients (.038 and .032) result. These lower order principal components in fact depend primarily upon emissivity differences. After the inverse rotation, variations in these components become color variations in the final product. Thus in Figure 9 color differences are indicative of emissivity differences in ground materials in the scene. These colors are modulated by

intensity variations which reflect topography, and hence are useful for establishing geographic orientation during interpretation. By comparison, in Figure 8 both color and intensity variations indicate emissivity differences.

In Figure 8, but particularly in Figure 9, we are now able to distinguish several rock types. Field checking of the image has revealed that most of the distinct color boundaries correspond to rock-type boundaries, although not all rock-type boundaries are distinguishable. In Figure 9, the color red is a good indicator of quartz content -- the more intense and "true" the red, the higher the quartz content. In general, the pink areas are silicified areas, sandy limestones, quartz latites, and quartz monzonites; the blues correspond to latites and monzonites and some carbonates; the purples to clays; and the green areas are carbonates, vegetation and alluvium.

It is not the intent of this paper to describe the geological interpretation of the images or their spectral significance. These are being described elsewhere. For instance, for a comparison of Figure 9 with a simplified geologic map, see Kahle and Rowan (1979). However, it is clear that with the image processing techniques used here, it is possible to separate several rock and ground-cover types based on their spectral emittance differences.

It is unfortunate, with the great potential shown here for geologic remote sensing, that the 24-channel scanner is no longer operational nor does there exist any other scanner with more than two mid-IR channels. This work reiterates and emphasizes the need for development of a multispectral, mid-IR scanner system for aircraft and satellite remote sensing.

ACKNOWLEDGMENT

J. B. Seidman and J. E. Conel contributed much useful advice while reviewing the manuscript. This paper presents the results of one phase of research carried out at the Jet Propulsion Laboratory, California Institute of Technology under contract NAS7-100, sponsored by the National Aeronautics and Space Administration.

REFERENCES

Gillespie, Alan R. and Anne B. Kahle, The Construction and interpretation of a digital thermal inertia image, Photogramm. Eng. Remote Sensing, 43, 983-1000, 1977.

Hovis, W. A., Jr., L. R. Blaine and W. R. Callahan, Infrared aircraft spectra over desert terrain 8.5u to 16u, Appl. Optics, 7, 1137-1140, 1968.

Hunt, G. R. and J. W. Salisbury, Mid-infrared spectral behavior of igneous rocks, AFCRL-TR-74-0625, 1974.

Hunt, G. R. and J. W. Salisbury, Mid-infrared spectral behavior of sedimentary rocks, AFCRL-TR-75-0356, 1975.

Hunt, G. R. and J. W. Salisbury, Mid-infrared spectral behavior of metamorphic rocks, AFCRL-TR-76-0003, 1976.

Kahle, Anne B. and Lawrence C. Rowan, Evaluation of multispectral middle infrared aircraft images for lithologic mapping in the East Tintic Mountains, Utah, submitted to Geology, 1979.

Lyon, R. J. P., Minerals in the infrared -- A critical bibliography, Stanford Research Institute, 1962.

Lyon, R. J. P., Analysis of rocks by spectral infrared emission (8 to 25 microns), Econ. Geol., 60, 715-736, 1965.

Lyon, R. J. P., Infrared spectral emittance in geological mapping: Airborne spectrometer data from Pisgah Crater, California, Science, 175, 983-986, 1972.

Ready, P. J. and P. A. Wintz, Information extraction, SNR improvement, and data compression in multispectral imagery, IEEE Trans. on Communications, Vol. COM-21, p. 1123-1131, Oct. 1973.

Selby, J. E. A., F. X. Kneizys, J. H. Chetwynd, Jr., and R. A. McClatchey,

Atmospheric Transmittance/Radiance: Computer Code LOWTRAN 4, AFGL-TR-78-0053, Hanscom AFB, Massachusetts, 100 pp, 1978.

Soha, J. M. and A. A. Schwartz, Multispectral histogram normalization contrast enhancement, Proc. Fifth Canadian Symposium on Remote Sensing, Victoria, B.C. Canada, 86-93,1978.

Taylor, M. M., Principal components colour display of ERTS imagery, Third Earth Resources Satellite-1 Symposium, NASA SP-351, 1877-1897, 1973.

Vickers, R. S. and R. J. P. Lyon, Infrared sensing from spacecraft: A geological interpretation. Thermophysics of Spacecraft and Planetary Bodies, Radiation Properties of Solids and the Electromagnetic Radiation Environment in Space, p. 585-607. G. B. Heller, ed., Academic Press, Inc., New York, 1967.

Vincent, R. K. and F. Thomson, Spectral Compositional Imaging of Silicate Rocks, J. Geophys. Res., 77, 2465-2472, 1972.

Vincent, R. K., F. Thomson, and K. Watson, Recognition of exposed quartz sand and sandstone by two-channel infrared imagery, J. Geophys. Res., 77, 2473-2477, 1972.

Vincent, R. K., Rock-type discrimination from ratio images of Pisgah Crater, California, Tech. Rpt. 31650-77-T, Willow Run Lab., 1972.

Vincent, R. K., A thermal infrared imaging method for mapping compositional variations among silicate rock types, Dissertation, University of Michigan, 1973.

Vincent, R. K., The potential role of thermal infrared multispectral scanners in geologic remote sensing, Proc. IEEE, 63, 137-147, 1975.

Vincent, R. K., L. C. Rowan, R. E. Gillespie, and C. Knapp, Thermal-infrared spectra and chemical analyses of twenty-six igneous rock samples, Remote Sensing of Environment, 4, 199-209, 1975.